Internal and external flow over laser-textured superhydrophobic PTFE

K. M. Tanvir Ahmmed, Christian Patience and Anne-Marie Kietzig[*]

McGill University, 3610 University Street, Montréal, Québec, H3A 0C5, Canada

KEYWORDS. Superhydrophobic surface, slip length, drag reduction, sphere, PTFE, femtosecond laser, laser-textured surface.

ABSTRACT. In this work, internal and external flows over superhydrophobic (SH) polytetrafluoroethylene (PTFE) were studied. The SH surface was fabricated by a one-step femtosecond laser micromachining process. The drag reduction ability of the textured surface was studied experimentally both in micro- and macro-scale internal flows. The slip length, which indicates drag reduction in fluid flow, was determined in micro-scale fluid flow with a cone-and-plate rheometer, whereas a pressure channel setup was used for macro-scale flow experiments. The textured PTFE surface reduced drag in both experiments yielding comparable slip lengths. Moreover, the experimentally obtained slip lengths correspond well to the result obtained applying a semi-analytical model, which considers the solid fraction of the textured surface. In addition to the internal flow studies, we fabricated SH PTFE spheres to test their drag reduction abilities in an external flow experiment, where the terminal velocities of the falling spheres were measured. These experiments were conducted at three different Reynolds numbers in both viscous and inertial

This document is the Accepted Manuscript version of a Published Work that appeared in final form in ACS Applied Materials & Interfaces. © 2016 American Chemical Society after peer review and technical editing by the publisher. To access the final edited and published work see ACS Articles on Request.

flow regimes with pure glycerol, a 30% glycerol solution, and water. Surprisingly, the drag on the SH spheres was higher than the measured drag on the non-SH spheres. We hypothesize that the increase in form drag outweighs the decrease in friction drag on the SH sphere. Thus, the overall drag increased. These experiments demonstrate that a superhydrophobic surface that reduces drag in internal flow might not reduce drag in external flow.

1. INTRODUCTION.

Superhydrophobic (SH) surfaces have gained a lot of attention in recent years because of their various properties, such as anti-wetting, anti-icing, anti-fogging, anti-corrosion, and self-cleaning [1-3]. SH surfaces are a result of both chemical hydrophobicity and surface roughness. These surfaces are characterized by their high apparent contact angle and low sliding angle, which are characteristic for the Cassie state of wetting [4]. When a water droplet sits on these surfaces, it sits on a composite surface of air and the material itself. The air-water interface is supported by the surface roughness features. When the water droplet moves, it slides on the shear-free air-water interface as well as the no-slip solid-water interface. The presence of the shear-free air-water interface reduces the friction drag in fluid flow. Thus, on a SH surface, the no-slip boundary condition at the wall no longer applies. An effective slip velocity on the surface represents drag reduction over a SH surface. This drag reducing property of SH surfaces attracted a large number of studies [5-8]. Many of these studies demonstrated promising drag reduction in laboratory scale experiments.

In many cases, the drag reduction is calculated from a measured effective slip length. The effective slip length of a surface is defined as the wall-normal distance into the wall, where the local velocity would vanish based on the velocity profile. The effective slip length is an area-averaged quantity. Though the effective slip length on a SH surface being much higher [9] compared to a smooth hydrophobic surface [10], determining the slip length is not a trivial task. Different measurement techniques have been employed to measure slip lengths on SH surfaces. The common techniques include but are not limited to parallel-plate rheometry [11-12], cone-and-plate rheometry [13], micro-particle image velocimetry (μ-PIV) [14-15], pressure drop measurements [6, 16-17], surface force apparatus experiments [18] and atomic force microscopy [19]. However, in most cases, the reported slip length values were measured using a single technique and not confirmed with another method. Moreover, many of these methods have an intrinsic source of error. For example, Bocquet et al. (2006) raised questions about the accuracy of rheometry measurements [20]. In addition, in PIV measurements, the uncertainty in locating the surface for rough samples needs to be recognized [8]. Thus, a comparative study of the two main methods, namely rheometry and pressure measurements, is lacking to affirm the drag reduction abilities of these surfaces.

Most of the research concerning slip length measurements on a surface was carried out with internal flow only, where friction drag dominates. The external flow on SH surfaces only recently gained attention [21]. In addition, to the best of our knowledge, none of the studies compared results from internal flow with those for external flow over a SH surface. The study of external flow behavior on such surfaces is important for large-scale applications such as submarines and ship hulls. Measuring the terminal velocity of a falling sphere is one of the easy ways to determine the drag reduction ability of a SH surface. However, previous results are not conclusive as summarized in Table 1. The change in terminal velocity or drag for the SH spheres compared to the non-SH spheres is also presented in the table. In addition to the experimental findings, theoretical analysis and numerical simulations were also conducted on the drag reduction obtained by SH spheres to gain more insight into the underlying mechanism [22-23]. Simulations predicted both increased and decreased drag with SH spheres depending on the thickness of the air layer and the flow pattern around the spheres. However, the only experimental evidence of increased drag with SH surface was attributed to the presence of bubbles (hemispherical caps) on the superhydrophobic surface [24].

Table 1. Previous experimental reports of drag on SH spheres.

Reports	Material	Liquid	Terminal velocity, mm/s	Reynolds number	% change
McHale et al. [25]	Solid acrylic spheres coated with hydrophobic sand	Water	420 – 560	$\sim 1\times10^4 - 3\times10^4$	5 – 15 [b]
Su et al. [24]	Hollow glass sphere coated with nanoparticles in a polymer	Water	382	$\sim 7\times10^3$	-5.9 [a]
Byon et al. [22, 26]	Oxidized copper spheres coated with Teflon®	Glycerol	9 – 14	<0.1	2 [a]
Brassard et al. [27]	Glass spheres coated with nanoparticles in a polymer	Water	720	$\sim 8\times10^3$	10 – 21 [b]

[a] % change in terminal velocity,

[b] % change in drag

In this study, we fabricated SH surfaces from a single material to use in both internal and external flow experiments. We chose to work with polytetrafluoroethylene (PTFE) because of its desirable properties, such as chemical, mechanical, thermal and biological stability, for various applications [28]. In addition, as PTFE is intrinsically hydrophobic, superhydrophobicity is achievable by simply altering its surface roughness. Thus, no coating or post-treatment is necessary. We textured the PTFE surface by femtosecond laser micromachining. We measured the slip lengths on the textured PTFE surface with a cone-and-plate rheometer and a pressure-driven flow channel and confirmed their drag reduction ability. Then, we tested textured PTFE spheres by dropping them in different fluids and found that the superhydrophobic spheres increased drag instead of decreasing it. We attributed this increased drag to the altered flow pattern around the textured superhydrophobic sphere that affects the form drag. For the first time, we showed that the slip lengths observed in internal flow tests do not guarantee that the same surface will also reduce drag for moving submerged objects.

2. MATERIALS AND METHODS.

2.1 Laser micromachining.

An amplified Ti:Sapphire laser system (Coherent Libra) was used to texture the surface. The laser system has a pulse duration of <85 fs, wavelength of 800 nm, and repetition rate of 1 kHz. A horizontally polarized Gaussian beam was focused on a sample with a 100 mm plano-convex lens. The $1/e^2$ theoretical beam diameter at focal plane was calculated to be 22 μm. We used commercially available polytetrafluoroethylene (PTFE) sheets and spheres (McMaster-Carr) for surface texturing. The sample was positioned at the focal plane on a computer controlled 3D translation stage (Newport Corporation). The translation stage along with the flat sample moved at a velocity of 12 mm/s under the stationary laser beam. Stage movement and shutter (Uniblitz) opening were controlled by the GOL3D software (GBC&S). The laser power was attenuated from 4 W to 54 mW by a computer controlled variable attenuator which consists of a half-wave plate and a polarizing beam splitter. Thus, the pulse fluence used in our experiment was 28 J/cm^2.

An overlap of 80% was maintained between two neighboring lines to fabricate a textured surface on an area larger than the beam diameter. However, to fabricate textured PTFE spheres, we changed the micromachining parameters. The stage velocity was reduced to 4 mm/s and scanned twice to account for fluence reduction due to the curved surface. The laser micromachining process was carried out in air. Samples were cleaned before and after laser micromachining in an ultrasonic acetone bath for five minutes.

2.2 Surface analysis.

The surface topography of the PTFE samples was imaged by scanning electron microscopy (SEM) (FEI Inspect F50). Prior to the SEM imaging, a gold coating of 10 nm thickness was applied to the ablated PTFE surface with a SPI-Module sputter coater. For imaging the surface of a textured sphere, we used a SU3500 scanning electron microscope (Hitachi) equipped with the Ultra Variable-Pressure (UVD) detector without any metal coating. The geometrical parameters of the ablated surface were measured by 3D confocal microscopy (Olympus LEXT OLS4000).

The air-water interface on the textured PTFE surface was imaged with a confocal laser-scanning microscope (Zeiss LSM 710). 40x and 63x water immersion lenses (Zeiss W Plan-Apochromat 40x/1.0DIC M27 and Zeiss W Plan-Apochromat 63x/1.0 M27) were used to obtain the images at different depths. ImageJ® software was used to stack the images and to obtain the Delaunay triangulation on the projected image.

Advancing and receding contact angles were measured with a goniometer (Data Physics OCA 15EC) at room temperature. An initial droplet size of 5 µL was used in the measurements. Separate syringes were used for the two test liquids (reverse osmosis (RO) water and 30% (w/w) glycerol solution) to avoid contamination. The droplet size was increased from the initial size of 5 µL to 8 µL with a dispense rate of 0.1 µL/s and then reduced to 5 µL at the same rate for dynamic contact angle measurements. The contact angle measurements were repeated three times for each sample.

2.3 Rheometer.

Slip lengths on the PTFE surfaces were determined by using a rheometer (Anton Paar MCR302) with a cone-and-plate measuring system (Fig. 4 (a)), for which the details were reported elsewhere [29]. PTFE discs of 1-inch diameter were mounted on the bottom plate, and three measurements were taken on each sample. The test liquids were placed between the sample and the bottom plate. The slip length was calculated from Eq. (1) [9] by measuring the torques at different shear rates. Shear rates were varied from 70 to 100 s^{-1}.

$$M = \frac{2\pi\mu\omega R^3}{3\theta}\left(1 - \frac{3\delta}{2R\theta} + \frac{3\delta^2}{R^2\theta^2}\right) - 2\pi\mu\omega\frac{\delta^3}{\theta^4}\ln\left(\frac{R\theta + \delta}{\delta}\right) \qquad (1)$$

In Eq. 1, M is the torque, μ is the viscosity of the liquid, ω is the angular velocity of the cone, R is the radius of the cone, θ is the cone angle, and δ is the effective slip length. It is to note that both the effective slip length and effective slip velocity are area-averaged quantities. Thus, the shear rate is uniform on the SH surface in a cone-and-plate geometry.

2.4 Pressure channel.

A horizontal rectangular channel was used to measure the drag reduction on the textured surfaces (Fig. 5 (a)). The channel was machined from an impact resistant polycarbonate slab. One side of the channel wall is replaceable with the textured surface. The channel is 10 mm in width, 1 mm in height and 300 mm in length. The pressure difference is measured in a test section of 30 mm length located 220 mm away from the entrance of the channel, thus eliminating the entrance effect. The pressure difference was measured with a digital pressure gauge (DPG 409-10WDWU, Omega). RO water was used as the working fluid and was driven by a gas pressure system. A tank filled with water was connected to a high-pressure N_2 gas cylinder. The flow rate was controlled by both the gas pressure and a needle valve installed in the flow line. The flow rate was measured with a turbine flow meter (FTB 504, Omega). The data was collected through a data acquisition system. The flow rate used in these experiments ranged between 400 to 600 mL/min corresponding to a Reynolds number of less than 2000, indicating laminar flow. The water temperature was measured with a thermocouple. The slip length was calculated by measuring the pressure drop at different flow rates by using the following equation for one-sided pressure driven channel flow [30]:

$$\delta = -\frac{2c\Delta D}{3 + 4\Delta D} \qquad (2)$$

where δ is the effective slip length, $2c$ is the channel height and ΔD is the change in drag, which was calculated by:

$$\Delta D = \frac{\Delta P - \Delta P_0}{\Delta P_0} \qquad (3)$$

where ΔP_0 and ΔP are the pressure gradients for the no-slip surface and the effective slip surface, respectively. Prior to experimentation, we verified the measurement accuracy of our flow channel setup by measuring the pressure drops at different flowrates in the laminar flow regime on a control surface. A non-SH flat PTFE surface was used as the control surface. The experimental measurements were consistent with the theoretical prediction as shown in Figure S1 of the supplementary information.

2.5 Terminal velocity experiments.

PTFE spheres with a diameter of 9.490 ± 0.009 (standard deviation) mm were used for the terminal velocity determination. The sphericity of the PTFE spheres were calculated and found to be 0.99. The physical properties of the spheres before and after laser ablation are tabulated in Table S1 in the supplementary information. We wetted the non-textured and the textured PTFE spheres before conducting the experiments to better compare our results with the air-retaining superhydrophobic textured spheres. We kept the spheres in pure ethanol to wet the surface. Then we transferred the spheres in the test fluid solution before dropping them for terminal velocity measurements. Two cylinders (19.7 cm inner diameter) filled with different fluids were used for the external flow experiments at intermediate Reynolds numbers. One of the cylinders was filled with RO water up to a height of ~2 m, whereas the other cylinder was filled with a 30% glycerol solution up to a height of ~0.5 m. A graduated cylinder filled with pure glycerol (≥99%, Sigma-

Aldrich) was used for the external flow experiments at a low Reynolds number. A Photron SA5 high-speed camera was used to capture the images of the falling spheres at 60 and 125 frames per second for the pure glycerol and 30% glycerol solution, respectively. We operated the camera at a shutter speed of 1/20,000 s for pure glycerol and 1/10,000 s for the 30% glycerol solution. We measured the distance travelled by the spheres at fixed time intervals from the images captured with the camera. Four replicates each with a new sphere were used for calculating the average terminal velocities. Only new spheres were used each time we dropped them into the fluid to avoid the post-experimental damage to the delicate SH sphere.

3. RESULTS AND DISCUSSION

3.1 Surface structures and wetting.

The textured PTFE sample is shown in Figure 1. The highly magnified images in Figure 1 (b and c) show that the surface is composed of micro and nano structures. The surface structures are nodular and fibrous in shape. The structures' size varied from a few micrometers to several hundred nanometers. The surface structures were well attached to each other and the pristine surface underneath. This was confirmed by sonicating the samples after micromachining and analyzing the SEM images, as the microstructures were still present on the sonicated sample. The effectively porous appearance of the laser-textured surface complicated traditional surface roughness measurements such as with a contact profilometer. Thus, we estimated the surface roughness from the non-contact 3D confocal microscopy measurements (Figure S2). The arithmetic average (R_a) and root mean square roughness (R_q) for the flat PTFE surface were 0.025 μm and 0.036 μm, respectively. In contrast, for the textured PTFE surface R_a and R_q were 0.262 μm and 0.323 μm, respectively. The roughness value on the PTFE sphere could not be confirmed because of technical limitations in measuring surface roughness on a spherical surface. However, we expected a similar surface structure on the PTFE sphere based on the results obtained with a wide range of laser machining parameters reported elsewhere [31]. We confirmed the similarity in surface structures in the SEM image shown in Figure S3 of the supplementary information.

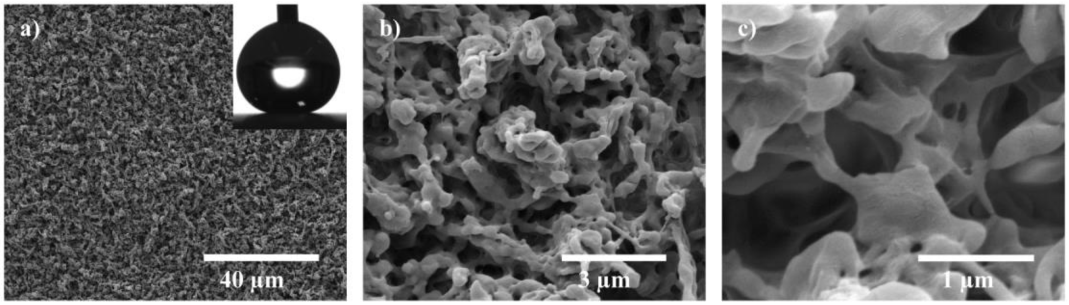

Figure 1. Scanning electron micrographs for the textured PTFE surface at different magnifications. Inset: water droplet sitting on the textured surface.

The textured PTFE surface showed advancing contact angles of 160 ± 1° and 158 ± 0°, whereas it demonstrated a contact angle hysteresis of 2 ± 1° and 3 ± 0° for water and 30% glycerol solution, respectively. The Cassie state of wetting prevailed on the surface as verified by the confocal microscopy image showing the air-water interface hanging between roughness valleys in Figure 2. Moreover, we analyzed the solid-water interface as shown in the montage of Figure S4 in supplementary information. By vertically stacking confocal microscopy images in ImageJ®, we calculated a wet solid fraction of ~9%.

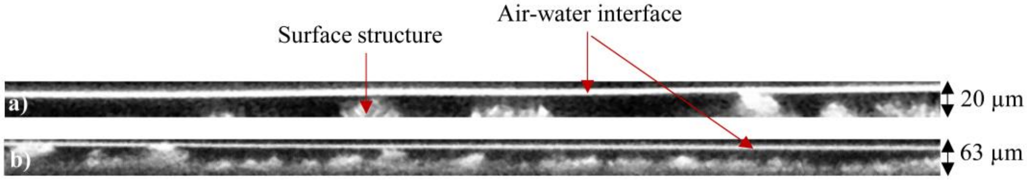

Figure 2. Air-water interface hanging between surface structures on a textured PTFE surface (side projection of the confocal microscopy images). (a) High and (b) low magnification images.

It is possible to compare this experimentally obtained solid fraction to the theoretically predicted solid fraction. The Cassie-Baxter equation (Eq. 4) relates the contact angle obtained on a textured surface (θ_c) to the solid fraction (f_1) of the surface and the contact angle obtained on a flat surface of the same material (θ_0) [32].

$$cos\theta_c = f_1 cos\theta_0 - 1 + f_1 \qquad (4)$$

The surface chemistry of textured PTFE does not differ significantly from the original non-ablated PTFE as reported elsewhere [33]. Thus, taking the water contact angle (θ_0) on a smooth PTFE surface to be 110° [34], we calculated a sold fraction of 10% from Eq. 4. This is in very good agreement with the experimentally measured (9%) solid fraction of the sample.

We tested the robustness of the surface both under dynamic and static condition. After flowing water over the textured surface at 700 mL/min there was no visible water penetration, meaning it remained SH. Further, a textured PTFE sphere was submerged in 4 ft of 30% glycerol solution to test its robustness under static condition. The silvery sheen around the sphere (Figure 3) confirms that no wetting transition occurred up to 12 kPa of pressure. It is important to note that the silvery sheen does not represent that the entire sphere surface was encased by an air layer. Instead, the sheen is created by the light reflection from the air-water interface hanging between the surface features as shown in Figure 2. In a separate experiment, a textured sphere was left submerged in ~1ft pure glycerol for four weeks to test the longevity of the surface; yet it still retained the trapped air. These evidences of air trapping confirmed that the air in the cavity did not deplete completely over a period of four weeks and more importantly that the surface is in the Cassie state of wetting for the entirety of the external flow experiment.

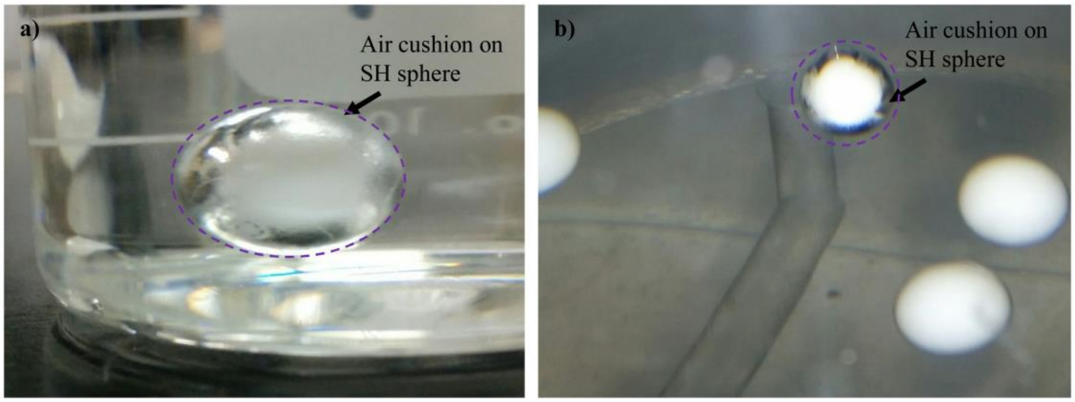

Figure 3. (a) A SH sphere in glycerol (>99%) and (b) a SH sphere with other non SH spheres in 30% glycerol solution. The SH sphere has a sheen around it (marked with dashed line) confirming the presence of trapped air between the surface features. The spheres are ~9.5 mm in diameter. The spheres look oval due to the curvature of the cylinder.

3.2 Internal flow.

We measured the slip lengths using two methods. The first method we used is based on torque measurements in a cone-and-plate rheometer as shown in Figure 4(a). The calculated slip lengths are plotted against shear rates on both SH PTFE and hydrophilic glass for water as well as 30% glycerol solution in Figure 4(b) and (c), respectively. The average slip length on SH PTFE with water was 17 ± 7 µm, while the slip length when using 30% glycerol solution was 38 ± 3 µm.

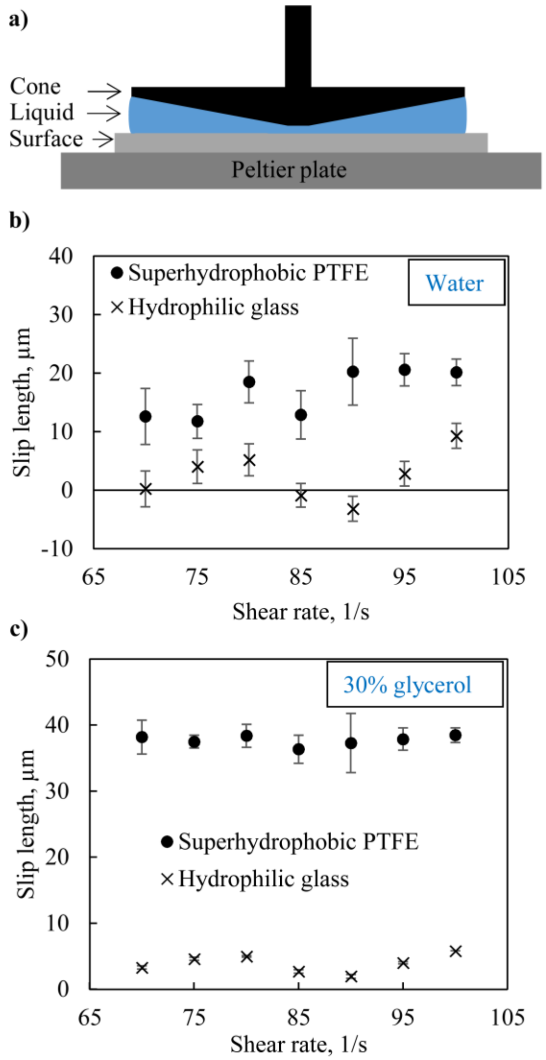

Figure 4. (a) Schematic of the rheometer setup. Measured slip lengths for (b) water and (c) 30% glycerol solution on both SH PTFE and hydrophilic glass. The error bars in the figure represent the standard errors for 3 replicates.

We observed higher slip length with the 30% glycerol solution compared to the slip length measured with water which is consistent with previous theoretical and experimental results [35-36]. In case of a surface covered with a plastron (air layer) of thickness *h*, the slip length depends on the viscosity of the liquid as estimated by Vinogradova (1995) [35]:

$$\delta = h\left(\frac{\mu}{\mu_g} - 1\right) \qquad (5)$$

where μ and μ_g are the viscosities of the liquid and the air layer, respectively. This proportionality of slip length with the liquid viscosity was experimentally confirmed by Choi et al. (2006) [36]. Thus, the ratio of the viscosity of water to the viscosity of 30% glycerol solution (~2.5) should equal the ratio of the slip lengths obtained with those two fluids. In our experiments, the latter ratio is 2.24, which indicates a slight deviation from the theoretical expectation. However, this difference is likely attributed to experimental error as the slip lengths obtained with the lower viscous fluid (water) in our experiment had higher variance (standard deviation, $\sigma = \pm 7$) compared to the slip lengths measured with the 30% glycerol solution ($\sigma = \pm 3$).

Our second method to measure slip length made use of a flow channel experiment (Figure 5(a)). The purpose of this second set of experiments was twofold. Firstly, to confirm that the PTFE surface reduces drag in a macro-channel, where the surface to volume ratio is less influential than in the microchannel, as represented by the rheometer experiments. Secondly, to establish a comparison of the measured slip lengths resulting from two independent methods.

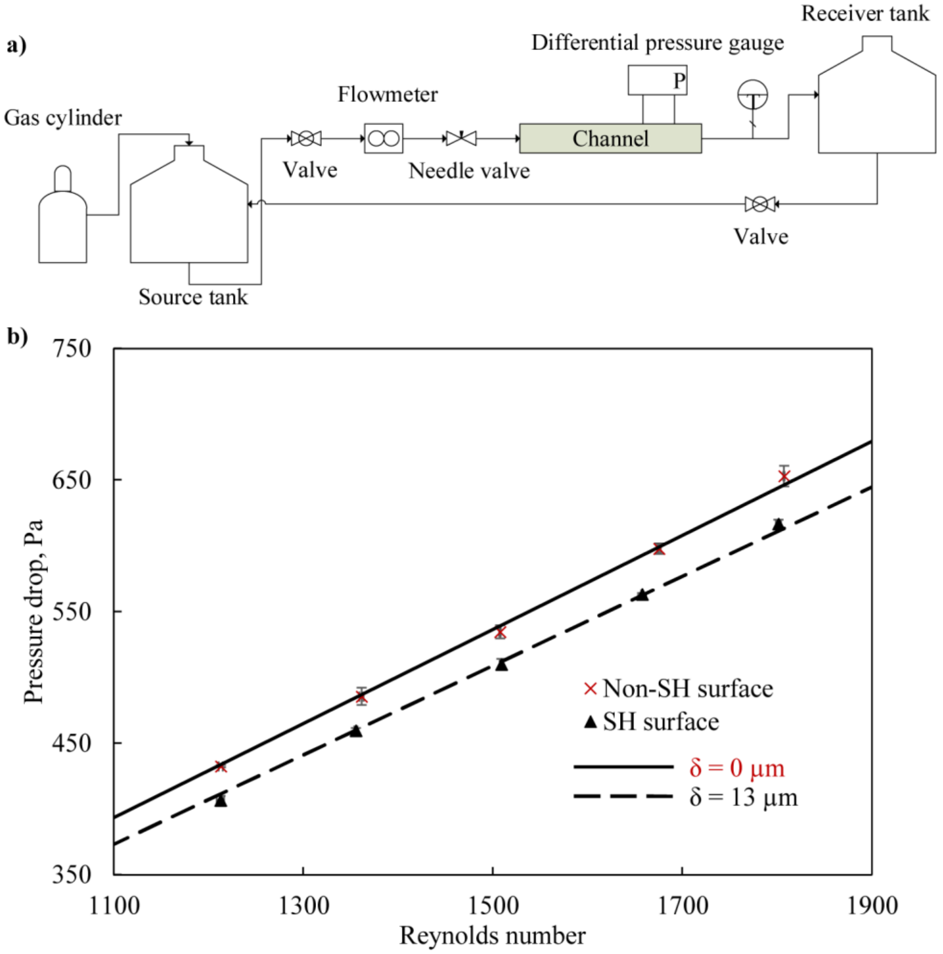

Figure 5. (a) Schematic of the flow channel setup. (b) Pressure drops in the flow channel at different Reynolds number for the non-SH surface and the SH surface (3 replicates). The displayed lines are the best fit of the experimental data for the tested surfaces. A slip length of 13 μm was calculated on the SH surface.

At the same Reynolds number, the measured pressure drop on the SH PTFE was lower than the pressure drop on the non-SH PTFE surface as shown in Figure 5 (b). A drag reduction of 5% was observed over the entire tested flow range. In addition, we calculated a slip length of 13 μm on the SH PTFE, which agrees well with the rheometer result of 17 ± 7 μm. It is important to mention that though slip flow constitutes only 5% of the total flow in this experiment, the contribution of the slip flow increases if we use a viscous fluid instead of water in a microchannel. For example, 30% drag reduction can be achieved in internal flow of 30% glycerol between two parallel plates with a 100 μm gap, where one of the plates is a textured PTFE surface.

We further compared our experimental results to a semi-analytical analysis. A few analytical and numerical models are available for predicting slip lengths on a regularly patterned sample [37-38]. However, no model is available for randomly patterned surfaces. As our surface structures are pillar-like (Figure 2), we choose a model for pillars arranged in a square lattice reported by Ng and Wang (2010) [39] to obtain a rough estimate of slip length for our randomly patterned sample:

$$\frac{\delta}{L} = \left(\frac{m}{\sqrt{\phi_s}} + n\right) \qquad (6)$$

where δ is the effective slip length, L is the periodicity, ϕ_s is the solid fraction, and m and n are fitting parameters from the numerical simulation with values of 0.34 and -0.468, respectively. We also note that a study similar to our study conducted by Srinivasan et al. (2013) correctly estimates the order of magnitude of the slip length for a randomly textured surface by using an analytical model for regularly patterned surfaces [12]. To calculate the slip length from Eq. 6, two parameters namely the solid fraction and the periodicity of the microstructures need to be measured. We previously calculated the solid fraction from the air-water interface image. Here, we used the air-water interface image again to locate the surface features in contact with the liquid to estimate the periodicity. The average periodicity (L) of 46 μm was calculated from the Delaunay triangulation of the wet microfeatures as shown in Figure 6 by using the Delaunay_Voronoi plugin in ImageJ®. Using this periodicity, we estimated a slip length of 28 μm, which is larger but of the same order of magnitude as our measured slip length (17 μm and 13 μm for water in the rheometer and the flow channel experiments, respectively).

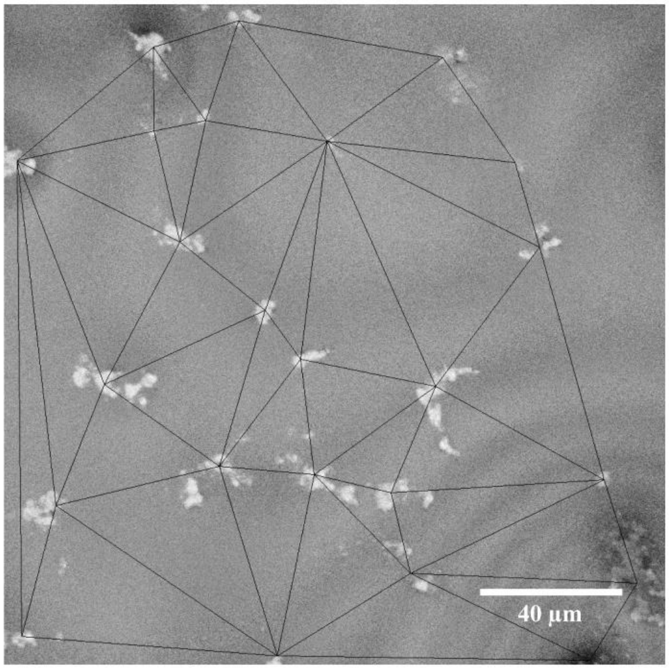

Figure 6. Projected view of the confocal microscopy images for the water droplet on the textured PTFE surface. Delaunay triangulation of the wet microfeatures was used to estimate the mean periodicity of the wetted surface features.

After comparing the results from two measurement methods and a semi-analytical estimation, we confirm that slip is certainly prevalent on our flat textured PTFE surface. This comparison was needed, as the measurement error from the rheometer experiment is high, especially when measuring a low slip length. However, from our slip length comparison we conclude that results from rheometer experiments with highly viscous liquids provide a representative estimate even for a surface with a small slip length.

3.3 External flow.

SH and non-SH PTFE spheres were dropped in a 30% glycerol solution and >99% pure glycerol (Figure 7 (a)). The positions of the falling spheres and the respective times were plotted in Figure 7 (b). The fitted straight line passing through the origin demonstrates that terminal velocity was reached.

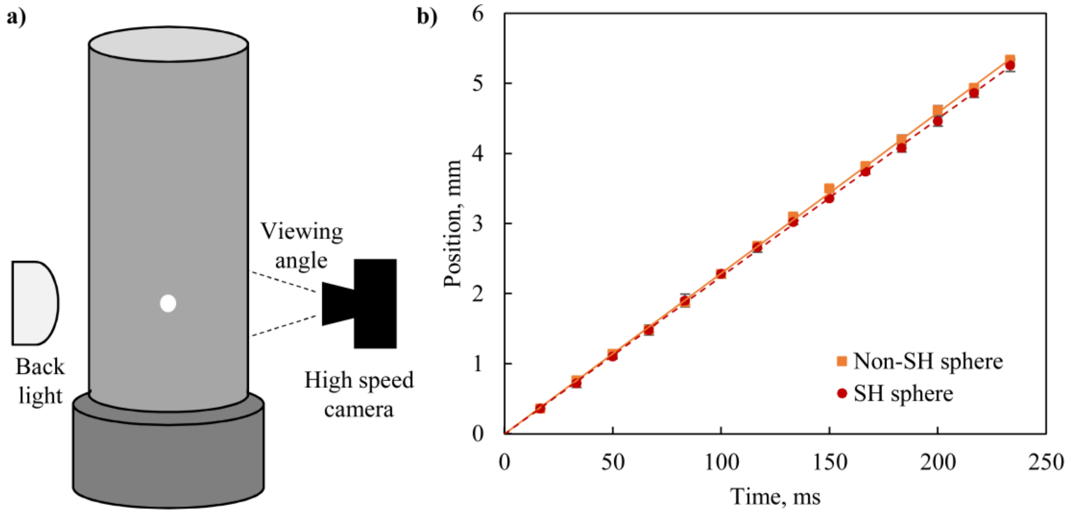

Figure 7. (a) Schematic of the experimental setup for terminal velocity measurements, (b) observed positions of the non-SH and SH falling spheres in pure glycerol are plotted against time to show that terminal velocity was indeed attained in the experiment (3 replicates).

The distances travelled in a set time interval by both the non-SH and SH spheres in pure glycerol are shown in Figure S5 in the supplementary information. We also conducted experiments with pre-wetted non-SH and SH spheres. The pre-wetted SH sphere lacks the air retention in their surface features. Thus, they allow us to compare the terminal velocities with air retention and without air-retention. However, the effective roughness of the pre-wetted and the non-pre-wetted SH spheres are not the same. On the pre-wetted sphere, the roughness is determined by the physical surface features (Figure 1), whereas on the non-pre-wetted sphere the roughness is dictated both by the air-water interface and the physical features (Figure 6).

The terminal velocities of SH and non-SH spheres in pure glycerol are plotted in Figure 8 (a) for both the non-pre-wetted and the pre-wetted conditions. While the average velocity of a SH sphere was slightly lower than the non-SH one, we found no statistically significant differences (ANOVA, F=2.9335, p=0.0767, α =0.05) in velocities between the non-SH and the SH spheres in both the pre-wetted and the non-pre-wetted states. In contrast, figure 8 (b) illustrates that a statistically significant difference (paired t test, t = -7.8461, p = 0.0002, α =0.05) exists in the velocities between the non-SH and the SH spheres in 30% glycerol solution in non-pre-wetted condition. The non-SH spheres moved 9% faster than the SH spheres. It is interesting to note that the pre-wetted SH sphere also had a lower average terminal velocity than the non-SH sphere. Moreover, the average terminal velocity of the pre-wetted SH spheres was higher than the air-retaining non-pre-wetted SH spheres.

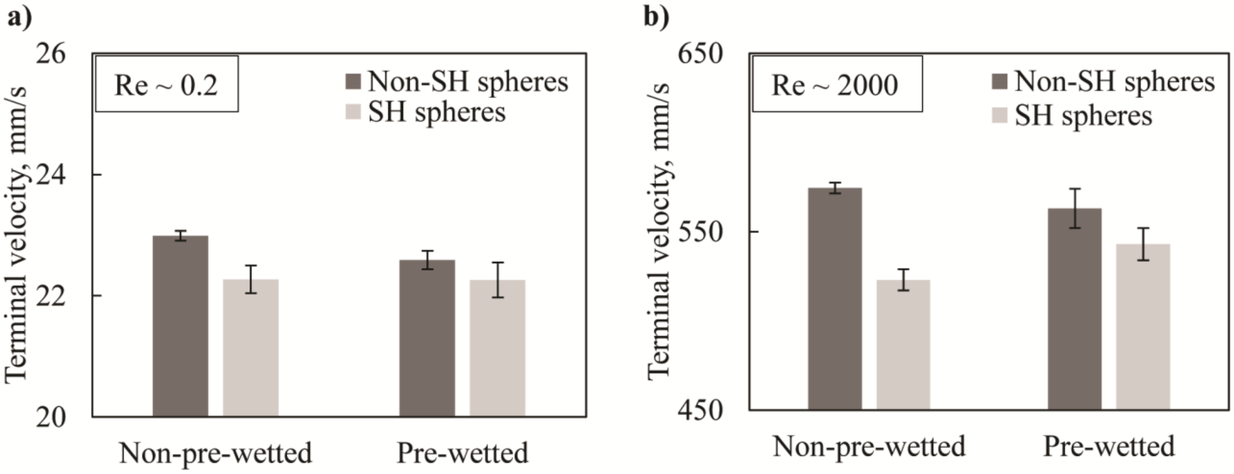

Figure 8. Experimental terminal velocities (4 replicates each with a new sphere) of non-SH spheres and SH spheres in (a) pure glycerol (>99%) and (b) 30% glycerol solution.

We compared our experimental results with theoretical predictions. The terminal velocities of the spheres in pure glycerol were corrected for the wall effect by using the empirical relation applicable in creeping flow proposed by Francis [40-41]:

$$u_t = u_{t\infty}\left(\frac{1-\lambda}{1-0.475\lambda}\right)^4 \qquad (7)$$

where u_t and $u_{t\infty}$ are the terminal velocities in a cylinder and in an infinite pool of water, respectively. λ denotes the ratio of the diameter of a sphere (d) to the diameter of a cylinder (D). Note that the experimental results conducted in 30% glycerol solution did not require any velocity correction factor as the Reynolds number was high (>2000) and the λ value was small (~0.05).

The corrected average terminal velocities in pure glycerol solution were 33.3 mm/s and 32.3 mm/s in non-pre-wetted condition for the non-SH and the SH spheres, respectively. Stokes' law ($F_d = 3\pi\mu du$) is used to calculate the theoretical terminal velocity (u), here F_d is the drag force, which is balanced by a net gravitational force acting on the sphere, and μ is the viscosity of the fluid. The calculated theoretical terminal velocity for the non-SH sphere was 32.2 mm/s. This is in very good agreement (error of ~3% and ~2% for the non-pre-wetted and the pre-wetted condition, respectively) with the experimental velocities (33.3 mm/s and 32.7 mm/s) considering that our experiments were carried out at the boundary (Re=0.2) of the applicable limit of Stokes' law [42], the purity of the glycerol is not exactly 100%, and that the velocity correction factor was derived from an empirical relationship.

After confirming our experimental result with the theoretical prediction for the non-SH spheres, we further analyzed the velocity differences between the non-SH and SH spheres. The SH spheres were slightly lighter and smaller compared to the non-SH spheres due to the laser machining process. Thus, while comparing the change in drag we used the theoretical predictions for an equivalent smooth sphere, which has a similar weight and size as the SH sphere. A detailed analysis of the difference in the net gravitational forces due to the weight and size difference of these two types of spheres is tabulated in Table 2. Accordingly, an equivalent smooth sphere with similar weight and size as the SH sphere is supposed to move 2% slower than the original non-SH sphere in pure glycerol (predicted difference in u, %). Our expectation from the internal flow experiments for a SH sphere was that it will reduce drag and that the sphere will move faster than that of the equivalent smooth sphere of a similar size. Surprisingly, no drag reduction was observed for the SH sphere, but rather an experimental difference in $u_{t\infty}$,% of -3% was observed.

Table 2. Forces acting on the spheres and their respective terminal velocities in different liquids. Change in predicted and experimental velocities are also calculated for the SH spheres compared to a Non-SH sphere in non-pre-wetted condition. We presented average values for clarity.

Liquid	Sphere type	Weight, N	Buoyancy force, F_b (N)	Net gravitational force, N	Predicted velocity, u (mm/s)	Experimental velocity, $u_{t\infty}$ (mm/s)	Predicted difference in u, %	Experimental difference in $u_{t\infty}$,%
Pure glycerol	Non-SH	0.00955	0.00549	0.00406	32.2	33.3[b]	-	-
	SH	0.00937	0.00542	0.00396	31.5[a]	32.3[b]	-2	-3
30% glycerol	Non-SH	0.00955	0.00472	0.00483	564	575	-	-
	SH	0.00937	0.00466	0.00471	560[a]	523	-1	-9
RO water	Non-SH	0.00955	0.00439	0.00516	609	604	-	-
	SH	0.00937	0.00433	0.00504	604[a]	543	-1	-10

[a] For an equivalent smooth sphere

[b] Corrected for wall effect

After observing no drag reduction in pure glycerol in low Reynolds number, we compared the terminal velocities for the non-SH and SH spheres in a 30% glycerol solution. We used a correlation proposed by Brown and Lawler (2003) to determine the drag coefficient (C_D) in the inertial flow regime [43]:

$$C_D = \frac{24}{Re}(1 + 0.15Re^{0.681}) + \frac{0.407}{1 + \frac{8710}{Re}} \qquad (8)$$

We estimated the terminal velocities (u) by using the following equation:

$$u = \left(\frac{8F_d}{\pi C_D d^2 \rho}\right)^{\frac{1}{2}} \qquad (9)$$

After comparing the terminal velocities of the original non-SH sphere and an equivalent smooth sphere of similar weight and size as the SH sphere, we calculated a merely 1% lower predicted difference in velocity for the equivalent smooth sphere due to the weight and size loss compared to the original non-SH sphere (Table 2). However, we found that the experimental terminal velocity of the SH sphere is 9% smaller compared to the original non-SH sphere. Thus, there was also no drag reduction for the SH sphere even at an intermediate Reynolds number.

Initially, we found the increased drag on the SH sphere in both low and intermediate Reynolds number to be confusing, because we had expected it to reduce as it did on the flat textured PTFE. However, other research groups (one experimental study and another numerical simulation) have already reported increased drag with SH spheres [24, 44]. Su et al. (2010) have observed micro- and nano-bubbles on the SH surface, which increased friction drag [24]. In our case, however, we did not notice any bubbles (hemispherical caps) from the confocal microscopy images. The low resolution of our confocal microscopy images might be unable to show small bubbles. Nevertheless, we observed reduced friction drag instead of increased friction drag in the flow cell experiment over a flat superhydrophobic PTFE surface, which further proves the absence of bubbles on the surface. Thus, our observations of drag increase with superhydrophobic spheres cannot be explained in the same way as Su et al. did.

Thus, we further investigated the mechanism of drag. The total drag on a sphere is composed of friction drag and form drag. The friction drag is due to the viscous shear stress, whereas the form drag is due to the pressure gradient across the sphere. Drag reduction on a superhydrophobic sphere occurs when the benefit of friction drag reduction outweighs the form drag increase, which was the case earlier reported by other researchers. Similarly, the effective slip on our SH spheres reduced the friction drag, as evidenced from the results of the internal flow experiments. Even hydrophilic rough spheres (similar to our pre-wetted spheres) can reduce friction drag because of the recirculation flow in the roughness cavity as observed by Byon et al. (2010) [22, 26]. However, to explain the overall drag increase, we hypothesize that the form drag increased in our falling sphere experiments and was not compensated by friction drag reduction. We base our hypothesis on the work of Byon et al. (2010), who reported increased total drag due to increase in form drag by a numerical simulation on spheres with roughness features compared to a smooth sphere [22]. Moreover, it was reported that the form drag depends on alignment and size of the roughness features. The flow pattern around a rough sphere is different than the flow pattern around a smooth sphere. Thus, the pressure distribution and consequently the form drag varies. According to our experimental results, the friction drag on our SH spheres did not decrease enough to offset the increase in form drag. At low Reynolds numbers, both the friction drag and the form drag contribute to the total drag. In this low Reynolds number scenario, we reason that on our SH spheres the decrease in friction drag was balanced out by the increase in form drag. The net effect is that statistically there is no change in terminal velocity for the SH sphere. However, at intermediate and higher Reynolds numbers the form drag dominates over friction drag. For example, a smooth sphere falling in water at $Re = 1\times10^3$ will have a friction drag of only 5% of the total drag [45]. Thus, we expected that at higher Reynolds numbers, the drag coefficient on our SH spheres will increase and consequently the terminal velocity will decrease. This is consistent with our experimental findings from the sphere dropping in 30% glycerol solution where the Reynolds number was $Re \sim 2\times10^3$. To confirm our hypothesis, we conducted another set of falling sphere experiments in RO water and thus at an even higher Reynolds number of $Re \sim 5\times10^3$. We observed a ~10% decrease in experimental terminal velocity (Table 2). The increase in form drag due to the roughness features was further confirmed by the lower terminal velocities in intermediate Reynolds number experiments for the pre-wetted SH spheres compared to the non-SH sphere. The difference in average terminal velocities between the pre-wetted and the non-pre-wetted SH spheres can be attributed to the difference in effective surface roughness of the SH spheres in two conditions as explained earlier.

Possible drag increase with SH spheres due to the increase in form drag was predicted in another numerical simulation conducted by Gruncell et al (2013) [44]. According to the simulation, the detailed surface geometry is more important than the average effect of the slip boundary condition when determining the drag reduction ability of a SH sphere. We measured an effective slip length on the flat PTFE, however, due to the difference in detailed surface geometry between a flat surface and a sphere that slip length did not translate into a net drag reduction in the external flow over the sphere. Thus, from our experimental results, we conclude that SH surfaces do not always reduce drag in external flow.

4. CONCLUSION

In this study, we tested the drag reduction abilities of laser textured superhydrophobic PTFE surfaces in both internal and external flow. The wetted solid fraction of the textured surface was determined by measuring the air-water interface with confocal microscopy. A theoretical estimate of the slip length was obtained by using the measured solid fraction. The slip length on the flat textured PTFE surface was measured by a cone-and-plate rheometer. This measurement was independently verified by pressure drop measurements in a flow channel. Thus, the drag reduction ability of the flat textured PTFE surface was established in internal flow. In a separate experiment, the drag reduction ability of a SH PTFE sphere was tested. Surprisingly, the drag force increased with the textured spheres instead of reducing it. We hypothesized that though the friction drag was reduced by the textured SH spheres, the form drag increased because of the increase in roughness. Further experiments validated our hypothesis, by demonstrating that a higher Reynolds number results in higher drag. Thus, superhydrophobicity is not the only condition for reducing drag in submerged external flow. The flow profile around the object needs to be considered for drag reduction with superhydrophobic surfaces.

ACKNOWLEDGEMENT.

This research was funded by the Natural Sciences and Engineering Research Council of Canada (NSERC) and the Fonds de recherche du Québec–Nature et technologies (FRQNT). The authors acknowledge the help from the members of the surface engineering group at McGill.

ASSOCIATED CONTENT

Flow channel measurement verification, PTFE spheres' physical properties before and after texturing, roughness profile of the textured PTFE surface, montage of air-water interface on the textured PTFE surface, SH and non-SH spheres falling through pure glycerol. This material is available free of charge via the Internet at http://pubs.acs.org.

Flow channel measurement verification

We calculated the theoretical pressure drop with the following equation:

$$Q = -\frac{4}{3\mu}\frac{\Delta P}{L}bc^3\left[1 - \frac{6c}{b}\sum_{k=1}^{\infty}\frac{\tanh\left(\frac{\alpha_k b}{c}\right)}{\alpha_k^5}\right] \qquad (S1)$$

where $\alpha_k = (2k-1)\frac{\pi}{2}, k = 1,2,\ldots$; Q is the volumetric flowrate, $\frac{\Delta P}{L}$ is the pressure gradient, $2b$ is the width of the channel, $2c$ is its height, and μ is the viscosity of the liquid. This theoretical prediction is plotted along with the experimental results in Figure S1.

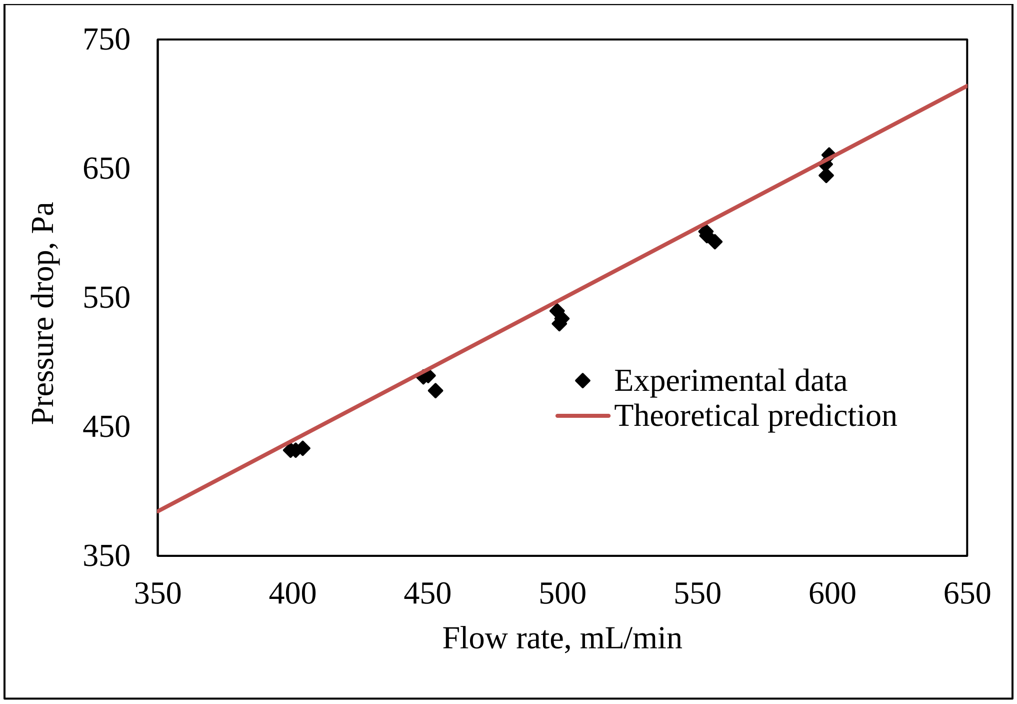

Figure S1. The accuracy of the measurements was verified in the flow channel with a non-SH flat PTFE control surface. The experimental data are from three sets of experiments. The solid curve is the theoretical prediction calculated from the physical geometry of the channel and the fluid properties.

PTFE spheres' physical properties before and after texturing

Table S1. Physical properties of the PTFE spheres, before and after ablation.

Parameters	Original	After ablation
Weight, g	0.9731 ± 0.0004	0.9555 ± 0.0012
Diameter, mm	9.490 ± 0.009	9.450 ± 0.012

Surface topographies of the textured PTFE surfaces.

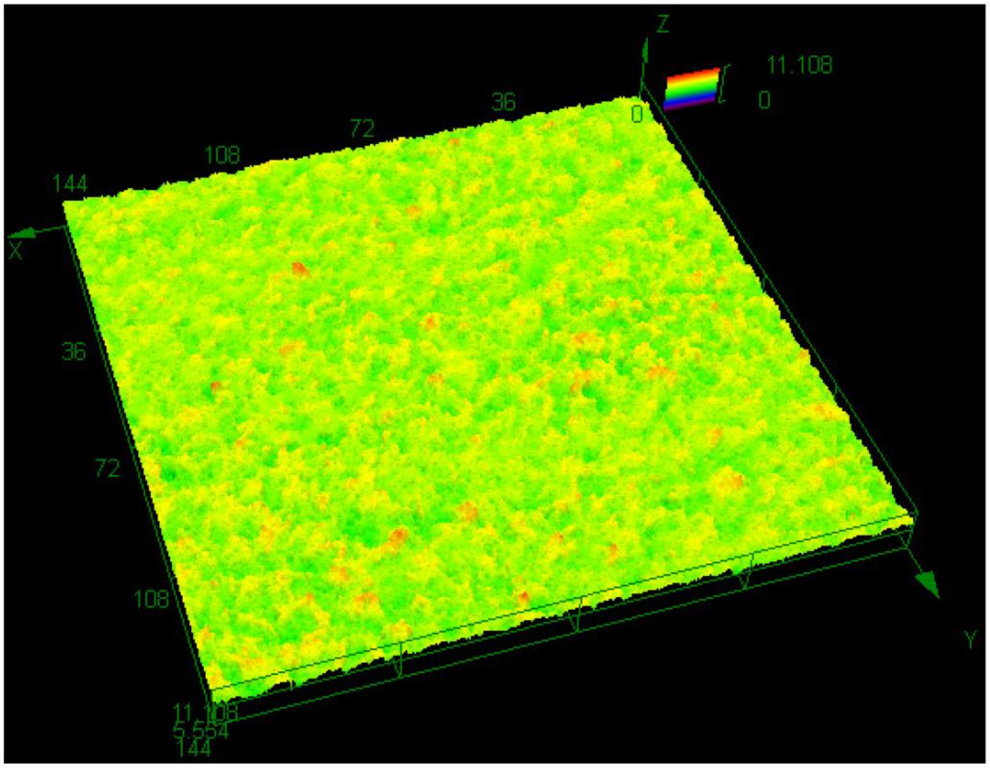

Figure S2. 3D roughness profile of the textured PTFE flat surface. Root mean square height of the surface $S_q = 0.7$ µm, maximum height of peaks, $S_p = 3$ µm, maximum height of valleys, $S_v = 7$ µm.

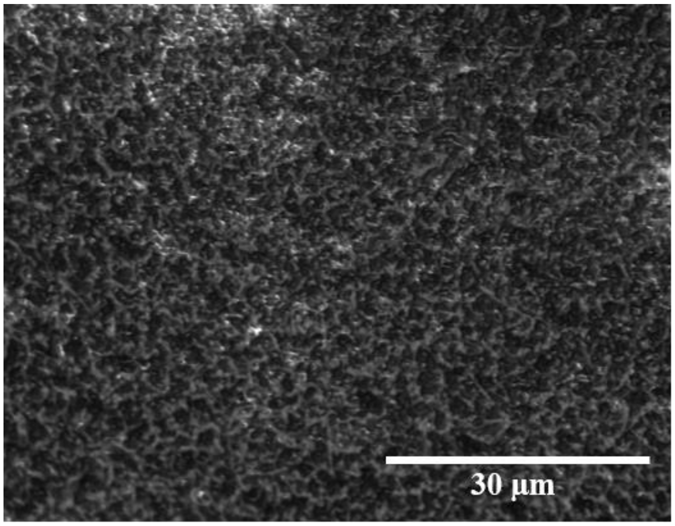

Figure S3. SEM image of the textured PTFE sphere.

Air-water interface.

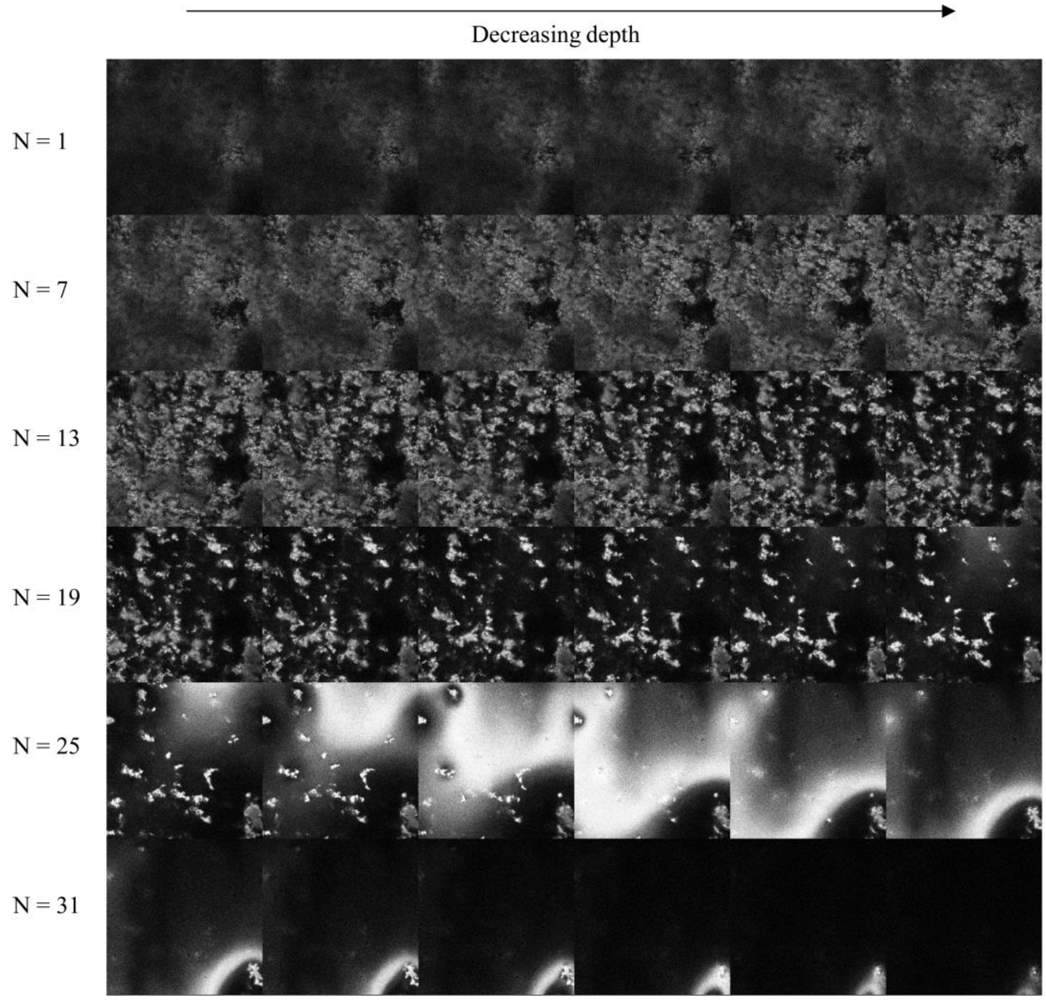

Figure S4. Montage of air-water interface determination with confocal microscopy. A total of 36 images are shown in the order of decreasing depth. N indicates the image number, where N=1 is the highest depth, and N= 36 is the lowest depth. The change in depth is 1.366 µm between two consecutive images. Each image is 192 µm × 192 µm in size.

SH and non-SH spheres falling through pure glycerol.

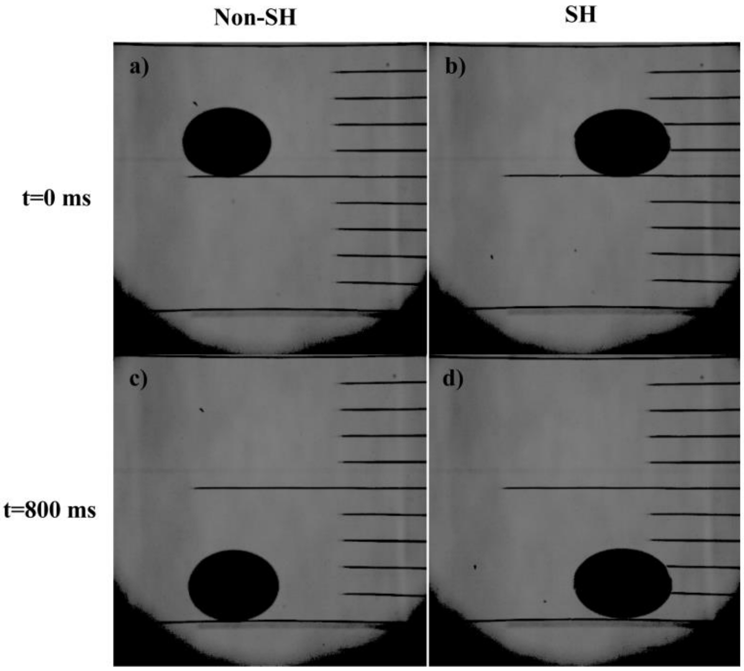

Figure S5. Two spheres falling through pure glycerol. (a) and (b) show the non-SH PTFE sphere and SH PTFE sphere, respectively. (c) and (d) show the same PTFE spheres after 800 ms. The diameter of the spheres are ~9.5 mm. The spheres look oval because of the curvature of the cylinder.

AUTHOR INFORMATION

Corresponding Author

* Tel: +1(514) 398-3302. E-mail: anne.kietzig@mcgill.ca

Author Contributions

K. M. Tanvir Ahmmed wrote the manuscript, designed and conducted all the experiments, and all the analyses. Christian Patience helped in setting up the sphere drop experimental rigs, participated in part of the sphere drop experiments and edited the manuscript. Dr. Anne-Marie Kietzig supervised the work and edited the manuscript.

Notes

The authors declare no competing financial interest.

REFERENCES

1. Zhang, Y. L.; Xia, H.; Kim, E.; Sun, H. B., Recent developments in superhydrophobic surfaces with unique structural and functional properties. *Soft Matter* **2012,** *8* (44), 11217-11231.

2. Yao, L.; He, J. H., Recent progress in antireflection and self-cleaning technology - From surface engineering to functional surfaces. *Prog. Mater Sci.* **2014,** *61*, 94-143.

3. Darmanin, T.; Guittard, F., Recent advances in the potential applications of bioinspired superhydrophobic materials. *J. Mater. Chem. A* **2014,** *2* (39), 16319-16359.

4. Bormashenko, E., Progress in understanding wetting transitions on rough surfaces. *Adv. Colloid Interface Sci.* **2015,** *222* (0), 92-103.

5. Ou, J.; Perot, B.; Rothstein, J. P., Laminar drag reduction in microchannels using ultrahydrophobic surfaces. *Phys. Fluids* **2004,** *16* (12), 4635-4643.

6. Daniello, R. J.; Waterhouse, N. E.; Rothstein, J. P., Drag reduction in turbulent flows over superhydrophobic surfaces. *Phys. Fluids* **2009,** *21* (8).

7. Choi, C. H.; Ulmanella, U.; Kim, J.; Ho, C. M.; Kim, C. J., Effective slip and friction reduction in nanograted superhydrophobic microchannels. *Phys. Fluids* **2006,** *18* (8).

8. Park, S.-H.; Lee, S.; Moreira, D.; Bandaru, P. R.; Han, I.; Yun, D.-J., Bioinspired superhydrophobic surfaces, fabricated through simple and scalable roll-to-roll processing. *Sci Rep* **2015,** *5*, 15430.

9. Lee, C.; Kim, C. J., Maximizing the Giant Liquid Slip on Superhydrophobic Microstructures by Nanostructuring Their Sidewalls. *Langmuir* **2009,** *25* (21), 12812-12818.

10. Tretheway, D. C.; Meinhart, C. D., Apparent fluid slip at hydrophobic microchannel walls. *Phys. Fluids* **2002,** *14* (3), L9-L12.

11. Zhou, M.; Li, J.; Wu, C. X.; Zhou, X. K.; Cai, L., Fluid drag reduction on superhydrophobic surfaces coated with carbon nanotube forests (CNTs). *Soft Matter* **2011,** *7* (9), 4391-4396.

12. Srinivasan, S.; Choi, W.; Park, K.-C.; Chhatre, S. S.; Cohen, R. E.; McKinley, G. H., Drag reduction for viscous laminar flow on spray-coated non-wetting surfaces. *Soft Matter* **2013,** *9* (24), 5691-5702.

13. Lee, C.; Choi, C. H.; Kim, C. J., Structured surfaces for a giant liquid slip. *Phys. Rev. Lett.* **2008,** *101* (6), 064501.

14. Ou, J.; Rothstein, J. P., Direct velocity measurements of the flow past drag-reducing ultrahydrophobic surfaces. *Phys. Fluids* **2005,** *17* (10).

15. Truesdell, R.; Mammoli, A.; Vorobieff, P.; van Swol, F.; Brinker, C. J., Drag reduction on a patterned superhydrophobic surface. *Phys. Rev. Lett.* **2006,** *97* (4), 044504.

16. Maynes, D.; Jeffs, K.; Woolford, B.; Webb, B. W., Laminar flow in a microchannel with hydrophobic surface patterned microribs oriented parallel to the flow direction. *Phys. Fluids* **2007,** *19* (9).

17. Shirtcliffe, N. J.; McHale, G.; Newton, M. I.; Zhang, Y., Superhydrophobic Copper Tubes with Possible Flow Enhancement and Drag Reduction. *Acs Applied Materials & Interfaces* **2009,** *1* (6), 1316-1323.

18. Cottin-Bizonne, C.; Cross, B.; Steinberger, A.; Charlaix, E., Boundary slip on smooth hydrophobic surfaces: Intrinsic effects and possible artifacts. *Phys. Rev. Lett.* **2005,** *94* (5).

19. Maali, A.; Bhushan, B., Measurement of slip length on superhydrophobic surfaces. *Philos Trans A Math Phys Eng Sci* **2012,** *370* (1967), 2304-20.

20. Bocquet, L.; Tabeling, P.; Manneville, S., Comment on ``Large Slip of Aqueous Liquid Flow over a Nanoengineered Superhydrophobic Surface". *Phys. Rev. Lett.* **2006,** *97* (10), 109601.

21. Zhao, J.-p.; Du, X.-d.; Shi, X.-h., Experimental research on friction-reduction with super-hydrophobic surfaces. *Journal of Marine Science and Application* **2007,** *6* (3), 58-61.

22. Byon, C.; Nam, Y.; Kim, S. J.; Ju, Y. S.; Asme In *The Effect of Surface Treatment on the Drag Characteristics in Laminar Flow*, Proceedings of the Asme Micro/Nanoscale Heat and Mass Transfer International Conference, Vol 3, New York, Amer Soc Mechanical Engineers: New York, 2010; pp 315-321.

23. McHale, G.; Flynn, M. R.; Newton, M. I., Plastron induced drag reduction and increased slip on a superhydrophobic sphere. *Soft Matter* **2011,** *7* (21), 10100-10107.

24. Su, B.; Li, M.; Lu, Q. H., Toward Understanding Whether Superhydrophobic Surfaces Can Really Decrease Fluidic Friction Drag. *Langmuir* **2010,** *26* (8), 6048-6052.

25. McHale, G.; Shirtcliffe, N. J.; Evans, C. R.; Newton, M. I., Terminal velocity and drag reduction measurements on superhydrophobic spheres. *Appl. Phys. Lett.* **2009,** *94* (6).

26. Byon, C.; Nam, Y.; Kim, S. J.; Ju, Y. S., Drag reduction in Stokes flows over spheres with nanostructured superhydrophilic surfaces. *J. Appl. Phys.* **2010,** *107* (6), 3.

27. Brassard, J.-D.; Sarkar, D. K.; Perron, J., Studies of drag on the nanocomposite superhydrophobic surfaces. *Appl. Surf. Sci.* **2015,** *324* (0), 525-531.

28. Wolfs, M.; Darmanin, T.; Guittard, F., Superhydrophobic Fibrous Polymers. *Polym Rev* **2013,** *53* (3), 460-505.

29. Tanvir Ahmmed, K. M.; Kietzig, A. M., Drag reduction on laser-patterned hierarchical superhydrophobic surfaces. *Soft Matter* **2016,** *12* (22), 4912-4922.

30. Busse, A.; Sandham, N. D.; McHale, G.; Newton, M. I., Change in drag, apparent slip and optimum air layer thickness for laminar flow over an idealised superhydrophobic surface. *J. Fluid Mech.* **2013,** *727*, 488-508.

31. Liang, F.; Lehr, J.; Danielczak, L.; Leask, R.; Kietzig, A. M., Robust Non-Wetting PTFE Surfaces by Femtosecond Laser Machining. *Int. J. Mol. Sci.* **2014,** *15* (8), 13681-13696.

32. Cassie, A. B. D.; Baxter, S., Wettability of porous surfaces. *Trans. Faraday Society* **1944,** *40*, 546.

33. Falah Toosi, S.; Moradi, S.; Kamal, S.; Hatzikiriakos, S. G., Superhydrophobic laser ablated PTFE substrates. *Appl. Surf. Sci.* **2015,** *349*, 715-723.

34. Chen, W.; Fadeev, A. Y.; Hsieh, M. C.; Oner, D.; Youngblood, J.; McCarthy, T. J., Ultrahydrophobic and ultralyophobic surfaces: Some comments and examples. *Langmuir* **1999,** *15* (10), 3395-3399.

35. Vinogradova, O. I., Drainage of a Thin Liquid Film Confined between Hydrophobic Surfaces. *Langmuir* **1995,** *11* (6), 2213-2220.

36. Choi, C. H.; Kim, C. J., Large slip of aqueous liquid flow over a nanoengineered superhydrophobic surface. *Phys. Rev. Lett.* **2006,** *96* (6).

37. Ybert, C.; Barentin, C.; Cottin-Bizonne, C. c.; Joseph, P.; Bocquet, L. r., Achieving large slip with superhydrophobic surfaces: Scaling laws for generic geometries. *Phys. Fluids* **2007,** *19* (12), 123601.

38. Davis, A. M. J.; Lauga, E., Hydrodynamic friction of fakir-like superhydrophobic surfaces. *J. Fluid Mech.* **2010,** *661*, 402-411.

39. Ng, C. O.; Wang, C. Y., Apparent slip arising from Stokes shear flow over a bidimensional patterned surface. *Microfluid. Nanofluid.* **2010,** *8* (3), 361-371.

40. Francis, A. W., Wall Effect in Falling Ball Method for Viscosity. *J. Appl. Phys.* **1933,** *4* (11), 403-406.

41. Di Felice, R., A relationship for the wall effect on the settling velocity of a sphere at any flow regime. *Int. J. Multiphase Flow* **1996,** *22* (3), 527-533.

42. Fuerstenau, M. C.; Han, K. N., *Principles of Mineral Processing*. Society for Mining, Metallurgy, and Exploration: 2003.

43. Brown, P. P.; Lawler, D. F., Sphere Drag and Settling Velocity Revisited. *Journal of Environmental Engineering* **2003,** *129* (3), 222-231.

44. Gruncell, B. R. K.; Sandham, N. D.; McHale, G., Simulations of laminar flow past a superhydrophobic sphere with drag reduction and separation delay. *Phys. Fluids* **2013,** *25* (4), 043601.

45. Pritchard, P. J., *Fox and McDonald's Introduction to Fluid Mechanics, 8th Edition*. John Wiley & Sons: 2010.